

3D-Printed Biomimetic Hydroxyapatite Composite Scaffold Loaded with Curculigoside for Rat Cranial Defect Repair

Yiping Weng, Xiuchen Yuan, Shijie Fan, Weihao Duan, Yadong Tan, Ruikai Zhou, Jingbin Wu, Yifei Shen,* Zhonghua Zhang,* and Hua Xu*



Cite This: *ACS Omega* 2024, 9, 26097–26111



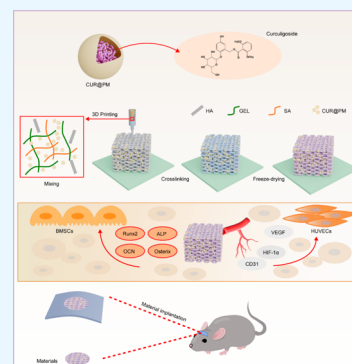
Read Online

ACCESS |

Metrics & More

Article Recommendations

ABSTRACT: The treatment of various large bone defects has remained a challenge for orthopedic surgeons for a long time. Recent research indicates that curculigoside (CUR) extracted from the curculigo plant exerts a positive influence on bone formation, contributing to fracture healing. In this study, we employed emulsification/solvent evaporation techniques to successfully fabricate poly(ϵ -caprolactone) nanoparticles loaded with curculigoside (CUR@PM). Subsequently, using three-dimensional (3D) printing technology, we successfully developed a bioinspired composite scaffold named HA/GEL/SA/CUR@PM (HGSC), chemically cross-linked with calcium chloride, to ensure scaffold stability. Further characterization of the scaffold's physical and chemical properties revealed uniform pore size, good hydrophilicity, and appropriate mechanical properties while achieving sustained drug release for up to 12 days. In vitro experiments demonstrated the nontoxicity, good biocompatibility, and cell proliferative properties of HGSC. Through alkaline phosphatase (ALP) staining, Alizarin Red S (ARS) staining, cell migration assays, tube formation assays, and detection of angiogenic and osteogenic gene proteins, we confirmed the HGSC composite scaffold's significant angiogenic and osteoinductive capabilities. Eight weeks postimplantation in rat cranial defects, Micro-computed tomography (CT) and histological observations revealed pronounced angiogenesis and new bone growth in areas treated with the HGSC composite scaffold. These findings underscore the scaffold's exceptional angiogenic and osteogenic properties, providing a solid theoretical basis for clinical bone repair and demonstrating its potential in promoting vascularization and bone regeneration.



1. INTRODUCTION

In the face of extensive bone defects arising from trauma, corrective surgeries, and excision of bone and soft tissue tumors, orthopedic surgeons encounter formidable challenges.¹ While autologous bone grafts have become the consensus for treating bone defects, concerns persist regarding the risks of immune rejection and infection associated with both autologous and allogeneic bone grafts.² These concerns stem from limited donor availability and the substantial time and cost requirements for such procedures.³ With the rapid evolution of bone tissue engineering, three-dimensional (3D) printing has found widespread applications in the field of bone defect repair. Ongoing efforts are dedicated to crafting an optimal, high-precision, and biodegradable scaffold that aims to exhibit impeccable control over drug release while maintaining a high degree of biocompatibility.^{4,5} This intricately designed scaffold serves as a template to precisely guide the regeneration of bone tissue.⁶ Additionally, it strives to strike a delicate balance between structural integrity and controlled drug delivery, emerging as a promising candidate for advancing the field of bone tissue engineering.⁷ However, existing bone repair scaffolds are confronted with certain challenges, such as limited biological activity, uncontrolled drug concentrations, and a sole bone-

filling function without bone-inductive capabilities, hindering the effective promotion of vascularization.^{8–10} Consequently, there is an imperative requirement to engineer multifunctional scaffolds capable of concurrently stimulating angiogenesis and osteogenesis. This development aims to improve the long-term stability and bone regeneration potential of these constructs.

The foundational materials for preparing drug-loaded scaffolds typically consist of nontoxic and biodegradable proteins or polymers such as collagen, chitosan, and poly(ϵ -caprolactone) (PCL), among others. Inorganic materials like hydroxyapatite (HA), tricalcium phosphate, montmorillonite, and bioactive glass can also be employed.^{11–14} Sodium alginate (SA), a natural anionic polysaccharide, exhibits unique gel properties upon cross-linking with calcium ions, making it suitable for the fabrication of three-dimensional mesh scaffolds.¹⁵ However, due to the lack of cell-adhesive sites in

Received: February 17, 2024

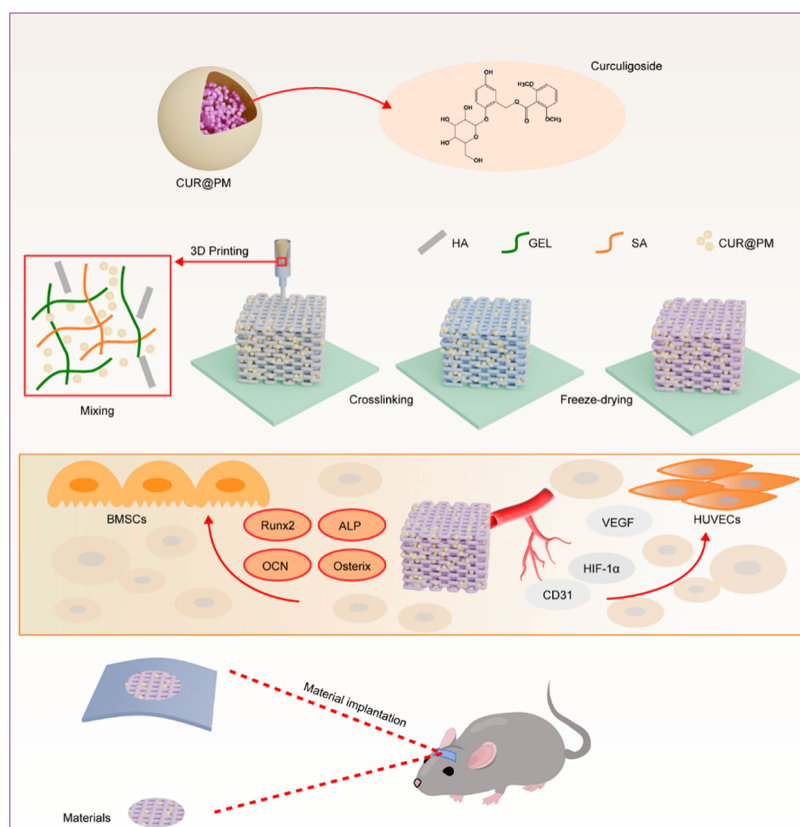
Revised: April 30, 2024

Accepted: May 10, 2024

Published: June 7, 2024



Scheme 1. Schematic Illustration of the Preparation of Composite Scaffolds Loaded with Curculigosome and Their Application in Bone Regeneration



sodium alginate itself, chemical modification or physical binding is needed to overcome its limitations.¹⁶ Physical modification, such as the approach taken by Liu et al., involving the incorporation of varying proportions of montmorillonite into gelatin and sodium alginate, has been demonstrated as a simple, cost-effective, and nontoxic method to enhance osteogenic properties.¹⁷ Hydroxyapatite (HA), a biologically active ceramic with a composition similar to human bone, is commonly used in the field of BTE due to its excellent biocompatibility and bone-inductive properties.¹⁸ However, its high brittleness restricts its application. Reports indicate that combining sodium alginate with hydroxyapatite can effectively improve the mechanical properties of the scaffold, making it suitable for bone repair materials.¹⁹ Gelatin (GEL), despite having good biocompatibility and nontoxicity, has shortcomings such as poor mechanical properties and easy degradation. By incorporating gelatin into a composite with sodium alginate and hydroxyapatite, we can significantly promote cell proliferation and adhesion and address mechanical deficiencies.¹⁴

Curculigosome (CUR), derived from the rhizomes of plants belonging to the *Curculigo* genus, is a critical bioactive phenolic compound.²⁰ It has been historically integrated into herbal treatments for osteoporosis since ancient times in China. Curculigosome ($C_{22}H_{26}O_{11}$) has been identified as the primary active component in *Curculigo* plants, despite the detection of flavonoids, plant sterols, and other phenolic compounds in these plants (Structure 1).

It should be noted that changes in the physicochemical properties of materials can subsequently impact cell responses. Tan et al. developed a pure drug-loaded scaffold. However, the combination of a pure scaffold with drugs may lead to unstable

drug release.²¹ Therefore, we are attempting to develop a sustained-release drug-loaded scaffold structure that can promote vascularization and bone growth at the site of bone defects. Poly(ϵ -caprolactone) (PCL) is a biocompatible and easily processable aliphatic polyester. Compared to commonly used drug carrier materials such as polylactic acid and poly(lactic-*co*-glycolic acid), PCL possesses superior characteristics.²² This is because the degradation rate of the former material is unstable, making it more prone to locally produce acidic degradation products, thereby increasing the risk of local acidosis.²³ To alleviate these potential issues, this study chooses PCL as the material for microspheres.

The objective of this study was to fabricate a 3D-printed hybrid scaffold composed of HA/GEL/SA/CUR@PM (HGSC) with a biomimetic dual-layer porous structure using the freeze-drying method. We employed an emulsification/evaporation method to prepare PCL porous nanomicrospheres loaded with curculigosome (CUR@PM), which were then incorporated into the HA/GEL/SA composite scaffold for controlled release of curculigosome. The biological activity of curculigosome in promoting vascularization and bone regeneration was harnessed to optimize the osteogenic effects of the hydroxyapatite composite scaffold (Scheme 1). Through in vitro experiments, we evaluated the cytotoxicity and biocompatibility of the scaffold while simultaneously assessing the levels of osteogenic and angiogenesis-related genes and proteins. These findings have profound implications for the promotion of vascularization and improvement of bone regeneration by HGSC. Furthermore, intriguingly, micro-computed tomography (CT) and histological analysis revealed significant bone repair capability and angiogenic effects in the rat cranial defect

area 8 weeks after implantation of the scaffold. In summary, this study boldly combines plant-derived bioactive compounds with modern bone tissue engineering, offering a novel direction for repairing large-scale bone defects in clinical settings.

2. MATERIALS AND METHODS

2.1. Materials. The gelatin (GEL), sodium alginate (SA), and hydroxyapatite (HA) used in this study were procured from Aladdin Biochemical Technology Co., Ltd. (Shanghai, China). Curculigoside (CUR) and polycaprolactone (PCL) were obtained from Yuan Ye Biotechnology Co., Ltd. (Shanghai, China). Dichloromethane (DCM) and dimethyl sulfoxide (DMSO) were supplied by Merck & Co., Inc. (Shanghai, China), while phosphate-buffered saline (PBS) was purchased from Solarbio. Dulbecco's modified Eagle's medium (DMEM), 5% v/v fetal bovine serum (FBS), and 1% v/v penicillin/streptomycin (P/S) were acquired from Thermo Fisher Biochemical Products Corporation (Shanghai, China).

2.2. Methods. **2.2.1. Preparation of PCL Curculigoside Nanomicrospheres.** PCL nanomicrospheres loaded with curculigoside (CUR@PM) were prepared using the traditional oil/water (O/W) emulsion/solvent evaporation technique. In brief, PCL (100 mg) was dissolved in DCM (5 mL), and the solution was sonicated for 1 h in a water bath (110 W, 35 Hz). The carefully weighed CUR (233 mg of drug powder) was added to the solution to achieve a final concentration of 100 mM.²⁰ Subsequently, the mixture was dripped into a poly(vinyl alcohol) (PVA) solution (2.0 w/v %) to form an emulsion. The emulsion was stirred at 500 rpm at room temperature for 3 h until the organic solvent completely evaporated, resulting in hardened microspheres. The nanomicrospheres were then washed three times with deionized water to remove residual surfactant, collected by centrifugation at 11,000 rpm (Sigma2-16p, Germany), and finally freeze-dried overnight. These particles were stored in a refrigerator at 4 °C ($n = 3$). The preparation of PM without CUR was similar and is not described further.

2.2.2. Preparation of Composite Scaffolds. The HGSC composite scaffold was prepared using the freeze-drying method. In brief, 2 wt % HA, 2 wt % SA, and 6 wt % GEL were prepared in ultrapure water and mixed at a 1:1:1 ratio. The mixture was stirred using a magnetic stirrer, and CUR@PM was added. The prepared bioink was loaded into a 3DDiscovery bioprinter (Regen Hu Ltd.) and printed using a DD135-N nozzle with a diameter of 0.33 mm, a printing speed of 3.6 mm/s, and a pressure range of 0.40–0.45 MPa. Finally, composite scaffolds with dimensions of 7.0 mm (diameter, \varnothing) \times 2.16 mm (height, h), suitable for a rat cranial defect model, were obtained. The HGSC composite scaffold containing CUR@PM was prepared as the experimental group, while the HGS scaffold without CUR@PM was prepared as the control group. Both scaffolds were immersed in a 2 wt % calcium chloride solution for cross-linking, with a duration of 8 h. Subsequently, they were washed three times with deionized water and freeze-dried overnight in a freeze-dryer (IlshinBioBase, located in Dongducheon, Korea) at -75 °C.

2.2.3. Characterization of CUR@PM and Composite Scaffolds. Morphological evaluation of the nanomicrospheres and scaffolds was conducted using scanning electron microscopy (SEM) (JSM-6360LA, Japan). Additionally, PM samples (50 mg) were dispersed in 10 mL of distilled water using ultrasonication (360 W, 10 s). The size distribution of the PM

was measured by dynamic light scattering (DLS) using a Zetasizer instrument (Malvern Co, U.K.).

2.2.4. Fourier Transform Infrared (FTIR) Analysis. Fourier transform infrared (FTIR) spectroscopy was used to analyze the functional group composition of the materials. The HGS/HGSC scaffold samples were flattened and placed in the spectrometer, which had a resolution of 4 cm^{-1} . Each sample was scanned three times to obtain spectral results in the range of $400\text{--}4000\text{ cm}^{-1}$.

2.2.5. Rheological Analysis of the Composite Biomaterial Ink. The feasibility of printing the bioink was evaluated using a TA Q500 HiRes system (TA Instruments). In brief, the bioink on the rheometer plate was subjected to small-amplitude oscillatory shear testing at 37 °C, with a shear rate ranging from 0 to 100 s^{-1} and a 5% strain amplitude. The storage modulus (G') and loss modulus (G'') were recorded over a temperature range of $10\text{--}45$ °C.

2.2.6. Water Absorption Test. Three scaffolds were randomly selected from each group and then weighed (W_A). Subsequently, they were immersed in distilled water at 37 °C for 24 h. After removing excess water, they were weighed again (W_B). The formula for calculating water absorption is as follows:

$$\text{water absorption ratio (\%)} = \frac{W_B - W_A}{W_A} \times 100\%$$

Here, W_A and W_B represent the weights of the scaffold before and after immersion, respectively.

2.2.7. Evaluation of Degradation. Before starting the in vitro degradation test, all sample scaffolds were dried and weighed to determine W_O . Subsequently, all samples were immersed in PBS and kept at 37 °C for 3, 7, 14, and 28 days. At each time point, the samples were removed, dried, and reweighed to determine W_t . The test was repeated three times. The weight loss was calculated using the following formula:

$$\text{degradation (\%)} = \frac{W_O - W_t}{W_O} \times 100\%$$

2.2.8. Determination of the Drug Loading Rate of CUR@PM. First, 30 mg of CUR@PM was placed into a 15 mL centrifuge tube, 7 mL of dichloromethane (DCM) was added, and then 2 mL of dimethyl sulfoxide (DMSO) was added to ensure complete dissolution of the drug. After sonication of the mixture for 1 min, 10 mL of phosphate-buffered saline (PBS, pH 7.4) was added and stirred until DCM was completely evaporated. The samples were centrifuged at 11,000 rpm for 15 min, and the supernatant was collected and analyzed using a UV spectrophotometer at a wavelength of 310 nm. Drug loading was calculated using the following formula:

$$\text{loading rate (\%)} = \frac{\text{actual drug weight}}{\text{CUR@PM weight}} \times 100\%$$

2.2.9. In Vitro Drug Release Assay. The prepared CUR@PM microspheres and HGSC scaffolds were separately placed in 30 mL centrifuge tubes containing PBS (pH = 7.4) and incubated at a constant temperature of 37 °C. At predetermined time points, 2 mL of the supernatant was collected and replaced with fresh PBS to maintain a total volume of 30 mL. The drug release rate was determined using UV-visible spectroscopy and calculated using the following formula ($n = 3$):

Table 1. Primer Sequences for qPCR Analysis

gene	forward	reverse
GAPDH _(Human)	5'-AATGGGCAGCCGTTAGGAAA-3'	5'-GCGCCCAATACGACCAAATC-3'
VEGF	5'-AACCTCACAAAGCCAGCACATAG-3'	5'-CAAATGCTTTCTCCGCTCTGAACAAG-3'
CD31	5'-AGCCAGCAGTATGAGGACCAGTC-3'	5'-TCCAATGACAACCACCGCAATGAG-3'
GAPDH _(Mouse)	5'-CACCACCAACTGCTTAGC-3'	5'-TTCACCACCTTCTTGATGTC-3'
OCN	5'-TTCACCACCTTCTTGATGTC-3'	5'-CCTTATGCCCTCCTGCTTG-3'
ALP	5'-GCAGTATGAATTGAATCGGAACAAC-3'	5'-ATGGCCTGGTCCATCTCCAC-3'

$$\text{CUR released \%} = \left(\frac{\text{measured CUR released}}{\text{total CUR amount}} \right) \times 100\%$$

2.2.10. Evaluation of Mechanical Properties. The scaffolds were freeze-dried and placed directly on the testing platform. Compression tests were conducted on the samples at 37 °C, with a load of 0.1 N and compression speed of 0.1 mm/s, using a universal material testing machine (MTS SYSTEMS Co., Ltd., China). The stress–strain curve was calculated.

2.3.0. Cell Culture. Before the experiment, the composite scaffolds were sterilized using ethylene oxide gas. Mouse bone marrow mesenchymal stem cells (BMSCs) and human umbilical vein endothelial cells (HUVECs) (ATCC; Chinese Academy of Sciences, Shanghai, China) were cultured in Dulbecco's modified Eagle's medium (DMEM) supplemented with 10% fetal bovine serum (FBS) and 1% (v/v) penicillin–streptomycin (P/S) solution in a 5% CO₂ incubator at 37 °C. The medium was changed every 2 days, and cells were passaged when they reached 80% confluence for subsequent experiments. Scaffold extract (SE) was obtained according to the requirements of the International Organization for Standardization (ISO 10993-12). Briefly, sterile scaffolds were soaked in serum-free DMEM at a ratio of 0.1 g/mL. After incubation in a cell culture incubator for 48 h, the supernatant was collected, aseptically filtered, and stored at 4 °C after the addition of 10% PBS and 1% P/S.

2.3.1. Cell Adhesion. To assess the biocompatibility of the scaffolds with cells, we seeded BMSCs at a density of 1×10^5 cells per well onto the HGS and HGSC composite scaffolds and cultured them in 12-well plates for 24 h. After fixation with 4% paraformaldehyde for 1 h, the scaffolds were subjected to a graded dehydration process, followed by freeze-drying. Subsequently, scanning electron microscopy (SEM) was employed to examine the attachment of cells to the scaffolds.

2.3.2. Evaluation of Scaffold Toxicity and Proliferation Characteristics. To assess the impact of HGS/HGSC scaffolds on BMSC proliferation, a Cell Counting Kit-8 assay (Beyotime, China) was employed. BMSCs were seeded at a density of 4×10^3 cells per well in a 96-well plate and incubated with SE for 1, 3, and 7 days according to the manufacturer's instructions. The absorbance at 450 nm for each well was measured using a microplate reader. After 3 days of incubation with SE, a live/dead fluorescence staining assay (Invitrogen) was used to differentiate between viable and nonviable cells. Subsequently, proliferation assessment was conducted using the EdU (Invitrogen) assay kit. Cells were seeded at a density of 1×10^5 cells per well in a 96-well plate and incubated for 1 day. Subsequent steps for fluorescence staining were performed following the manufacturer's instructions. Stained cells were visualized using an inverted fluorescence microscope (Olympus IX 73, Japan).

2.3.3. Real-Time Quantitative Polymerase Chain Reaction (RT-qPCR). To conduct RT-qPCR following the methods previously described in our research group, in summary,

HUVECs and BMSCs were seeded on scaffolds at a density of 4×10^4 cells per well and cocultured for 3 and 7 days. Total RNA was extracted from the cells by repeatedly pipetting the scaffolds with TRIzol (500 μ L) reagent (TRIzol reagent, Invitrogen). Reverse transcription was performed using a reverse transcription kit (Vazyme, China). Finally, real-time fluorescence PCR was carried out using the SYBR Green quantitative PCR kit (Vazyme, China). The primer sequences for angiogenesis and osteogenesis genes are provided in Table 1.

2.3.4. Cell Migration and Tube Formation Experiments. In a 24-well plate, HUVECs were seeded at a density of 2×10^4 cells per well and cocultured with SE for 2 days to assess their migratory ability. Subsequently, images were captured ($n = 3$), and a quantitative analysis of cell migration was performed. To evaluate the scaffold's influence on tube formation capacity, HUVECs were seeded at a density of 4×10^4 cells per well onto a matrix gel (ABW Matrigel, China) in a 48-well plate and coincubated with SE culture medium for 7–8 h. Calcein-green (Invitrogen) fluorescence staining was conducted, and images were recorded using an inverted fluorescence microscope. Quantitative analysis included grid formation, node count, and branch count on the matrix gel for each group ($n = 3$).

2.3.5. Alkaline Phosphatase (ALP) and Alizarin Red Staining. In each well of a 6-well plate, 5.0×10^4 BMSCs were seeded and cultured in scaffold extract (SE) for 7 and 14 days. Subsequently, staining was performed using the ALP assay kit and Alizarin Red S staining kit (Beyotime, China).

2.3.6. Immunofluorescence Analysis. In the initial step, BMSCs were seeded at a density of 3×10^4 cells per well in a 12-well plate, followed by cultivation in scaffold extract (SE) for 3 days. Fixation was performed using 5% paraformaldehyde, permeabilization with 0.3% Triton X-100 solution, and blocking with 5% bovine serum albumin solution. Primary antibody (RUNX2, 1:100, Sanying Biotechnology, China) was incubated at 4 °C for 24 h. Subsequently, a secondary antibody conjugated with a fluorescent dye (1:200, Abcam) was applied for 45 min. After washing three times with PBS, staining was carried out using DAPI solution (Beyotime, China). Finally, fluorescence intensity was observed and quantitatively analyzed using an inverted fluorescence microscope (Olympus, Japan).

2.3.7. Western Blotting Assay. ²¹Following the established procedures in our research group for protein imprinting experiments, in brief, total proteins from BMSCs and HUVECs were individually extracted using the RIPA lysis method. The BCA Protein Assay Kit (Solarbio Beijing, China) was then employed for protein quantification. Subsequently, proteins underwent sodium dodecyl sulfate-polyacrylamide gel electrophoresis (SDS-PAGE) and were transferred onto nitrocellulose membranes. Overnight incubation at 4 °C was carried out with rabbit anti-HIF-1 α (1:2000), anti-VEGF (1:3000), anti-RUNX-2 (1:2000), and anti-Osterix (1:2000) antibodies. After three washes with TBST, the membranes were incubated with horseradish peroxidase-conjugated secondary antibodies

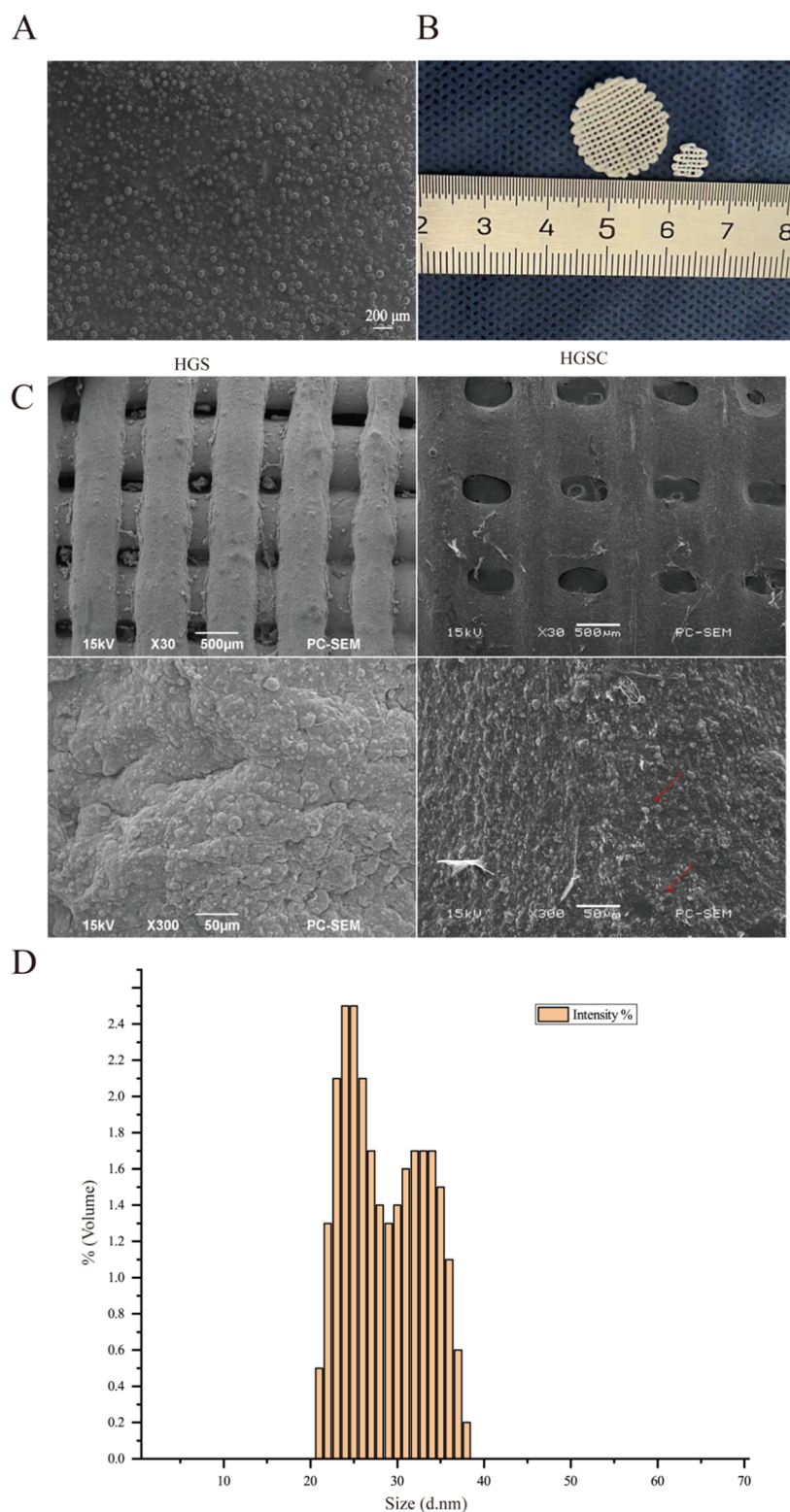


Figure 1. Scaffold characterization. (A) SEM image of CUR@PMs; (B) gross morphology of the different scaffolds; (C) SEM image of the scaffolds, with the CUR@PM indicated by the red arrow; and (D) size distribution of CUR@PM microsphere.

(1:4000) before protein imprint analysis using the ECL western blot detection system (Millipore). All antibodies were procured from Sanying Biotechnology (Wuhan, China). ImageJ software was employed for quantitative analysis of the immunoblot images.

2.3.8. In Vivo Experiment. To assess the in vivo efficacy of the composite scaffold in bone repair, we selected 15 Sprague–Dawley (SD) rats aged 8–10 weeks, with a weight of (210 ± 50) grams. They were randomly divided into three groups: blank control group, HGS group, and HGSC group. Initially, all rats underwent intraperitoneal injection of 3% pentobarbital (100

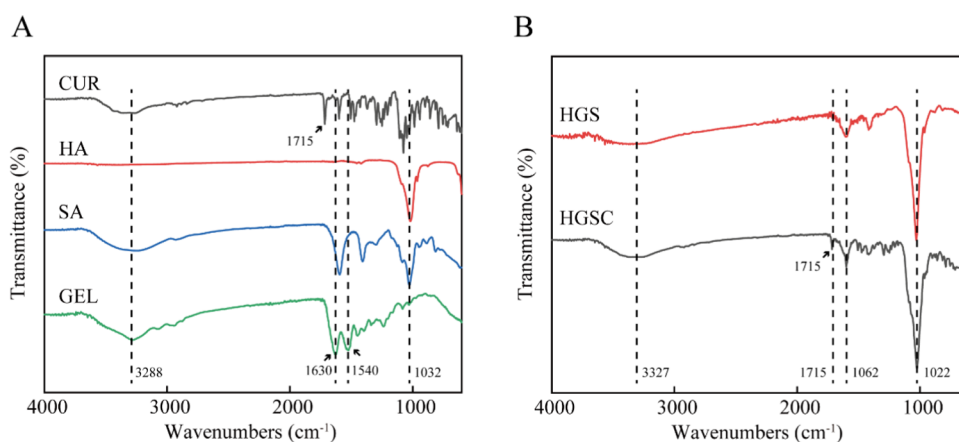


Figure 2. Infrared spectrum of the material. (A) Infrared spectroscopic analysis of CUR, HA, SA, and GEL; (B) composition analysis of HGS/HGSC scaffold.

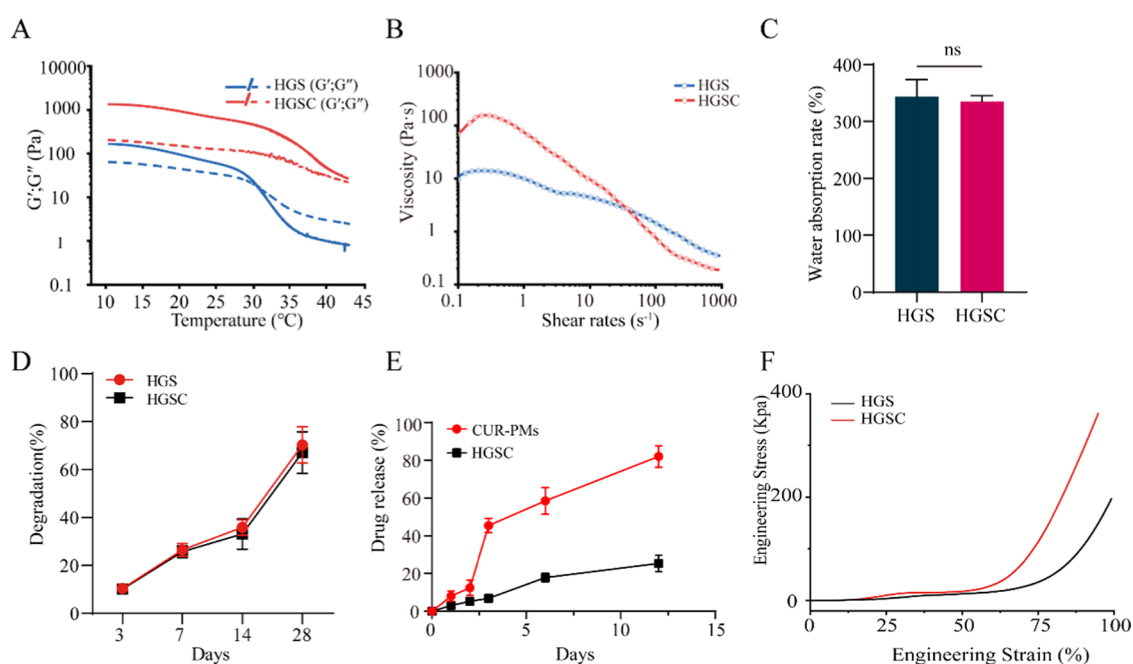


Figure 3. Physicochemical properties of HGS/HGSC composite scaffolds. (A) and (B) Rheological analysis of the scaffolds; (C) water absorption capacity of scaffolds ($n = 3$); (D) degradation of the scaffolds; (E) evaluation of curculigoside release from drug-loaded nanomicrospheres and microsphere-composite scaffolds; and (F) engineering stress–engineering strain curves for HGS/HGSC composite supports.

mg/kg) for anesthesia. Subsequently, the rat's scalp was disinfected, and a 1.5 cm incision was made at the center of the scalp to expose the skull. A cylindrical skull defect (diameter 8 mm) was created using an electric drill, and after clearing bone fragments, the scaffold was implanted into the defect. Finally, the incision was sutured layer by layer. All animal experiments followed the guidelines of the Institutional Animal Care and Use Committee (IACUC) and received approval from Jiangsu Science Standard Medical Detection Co., Ltd. (Approval No. IACUC22-0098).

2.3.9. Micro-CT Scanning and Tissue Staining Evaluation.

Using the SkyScan 1276 micro-CT scanner, we conducted detailed observations ($n = 3$) on rat skull repair at 8 weeks through micro-CT scanning and analysis. During the analysis, we focused on bone volume fraction (BV/TV) and cross-sectional trabecular number (Tb.N). To obtain comprehensive information, we subjected rat skull samples from each group to decalcification with 15% ethylenediaminetetraacetic acid

(EDTA) at room temperature for 35 days, with updates every 48 h. Subsequently, the samples underwent sequential ethanol dehydration and paraffin embedding, and were sectioned into 5 μ m thick slices. These slices were stained with hematoxylin and eosin (H&E) and Masson's trichrome for observation under an optical microscope (Olympus, Japan). Subsequently, to investigate the vascular generation activity of in situ vascularized tissue-engineered bone (TEB), in the immunofluorescence staining, the defatted tissue sections were blocked with 5% BSA in PBS-Tween. We utilized primary antibody Anti-CD31 (1:200, Abcam) and secondary antibody, Alexa Fluor 488-conjugated goat antirabbit (1:500). Finally, observation was conducted using an inverted fluorescence microscope (Zeiss, Oberkochen, Germany).

2.3.10. Statistical Analysis. All data are presented as the mean \pm standard deviation. One-way analysis of variance (ANOVA) was used to evaluate significant differences between the two groups. * $P < 0.05$ (*), ** $P < 0.01$ (**), and *** $P <$

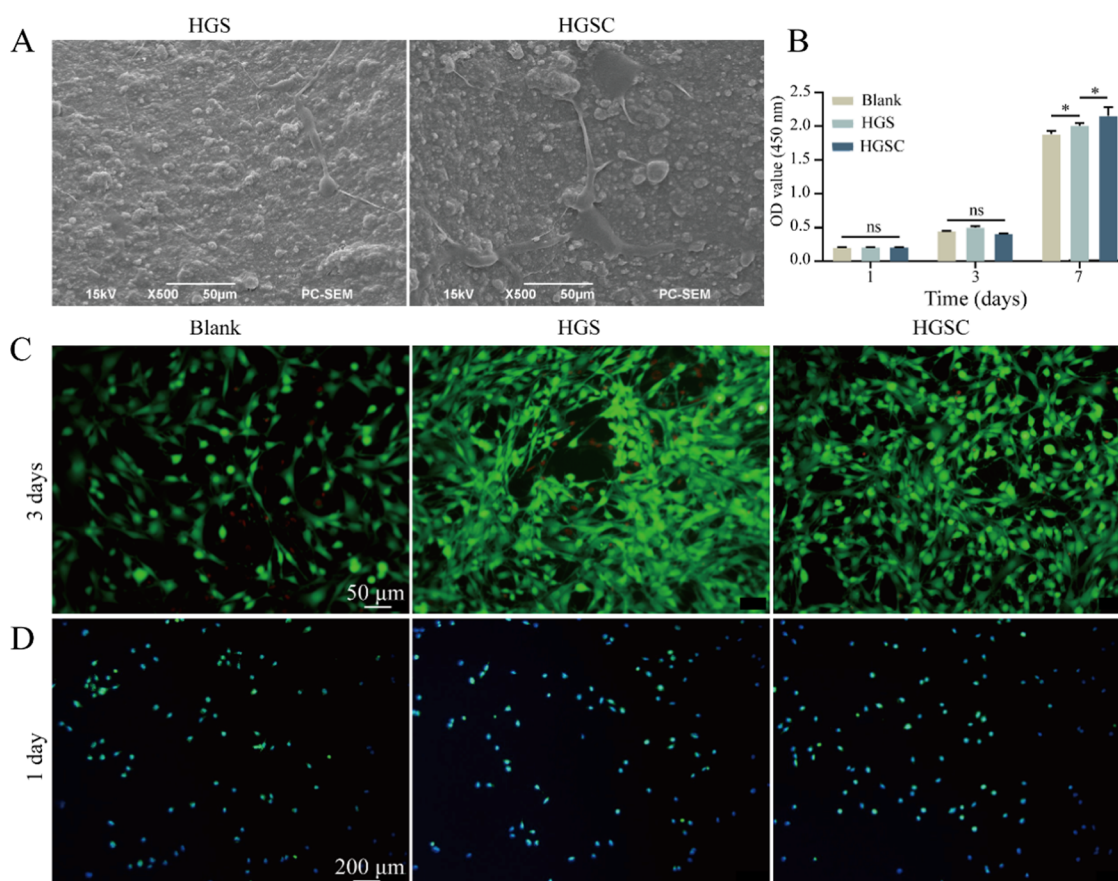


Figure 4. Evaluation of the biocompatibility of scaffolds. (A) SEM images of cells seeded on the different scaffolds for 3 days ($n = 3$); (B–D) evaluation of scaffold biotoxicity using CCK-8, Live/dead staining, and EdU staining ($*P < 0.05$, $n = 3$).

0.001 (***) were considered statistically significant. Origin 8.0 software (OriginLab Corporation) and GraphPad Prism 9.1 software were used for statistical analyses.

3. RESULTS

3.1. Characterization of CUR@PM and Composite Scaffolds. Based on the SEM results, CUR@PM exhibits a spherical shape with a smooth surface and uniform size (Figure 1A). Figure 1B depicts a macroscopic view of the 3D-printed scaffold. The surface of the HGS/HGSC composite scaffold is rough, with uniform pore sizes. It is worth noting that the pore size of the scaffold directly affects the transport of nutrients in the local tissue. In the local area of HGSC, dispersed CUR@PM can be observed (Figure 1C). According to dynamic light scattering (DLS) measurements, the size of the nanomicrospheres primarily falls within the range of 15.7 ± 14 nm (Figure 1D).

3.2. FTIR Analysis. In the infrared spectrum of curculigoside (CUR), strong peaks at approximately $1700\text{--}1750$ cm^{-1} can be observed, which may be attributed to carbonyl ($\text{C}=\text{O}$) vibrations. Hydroxyapatite exhibits significant peaks distributed at approximately 1010 cm^{-1} , primarily due to the stretching and bending vibrations of phosphate groups. Sodium alginate ($-\text{COO}-$) characteristic peaks appear at approximately 1600 and 1400 cm^{-1} . Additionally, a broad peak near 3300 cm^{-1} suggests the formation of hydrogen bonds. Gelatin's characteristic peaks were observed at 1630 cm^{-1} , and amide peaks were observed at 1540 cm^{-1} (Figure 2A). Based on Figure 2B, in the HGSC group, a characteristic peak of curculigoside can be observed at

approximately 1715 cm^{-1} , indicating the successful loading of the drug into the scaffold.²⁴

3.3. Rheological Analysis of the Composite Biomaterial Ink. To evaluate the suitability of the bioink for printing, rheological behavior tests were performed. In this study, the bioink containing HGSC had a storage modulus (G') higher than the loss modulus (G'') between 10 and 45 $^{\circ}\text{C}$, regardless of the temperature variation. However, the bioink containing HGS had a storage modulus (G') lower than the loss modulus (G'') at 30 $^{\circ}\text{C}$ (Figure 3A). Additionally, by measuring the flow properties of the two bioinks, we found that both exhibited shear-thinning behavior, with a decrease in viscosity as the shear rate increased, ensuring printing stability and flowability (Figure 3B).

3.4. Evaluating Scaffold Properties: Water Absorption, Drug Loading, Release, and Mechanics. Based on Figure 3C, there was no significant difference in water absorption between the two groups of scaffolds after the addition of CUR@PM. The degradation rate curve of the scaffolds showed a similar trend between the HGS scaffold and the HGSC scaffold. From day 3 to day 7, both scaffolds exhibited an accelerated degradation rate (Figure 3D). From day 7 to day 14, the degradation rate slowed, and from day 14 to day 28, there was another acceleration in the degradation rate. The drug loading rate of CUR@PM was found to be $16.98 \pm 2.23\%$. On day 3, CUR@PM and HGSC released $45.1 \pm 3.51\%$ and $6.86 \pm 1.05\%$ of the total drug, respectively. Finally, on day 12, it was observed that the drug release rate for CUR@PM was $82.0 \pm 4.9\%$, while for HGSC, it was $25.7 \pm 3.1\%$ (Figure 3E). The engineering

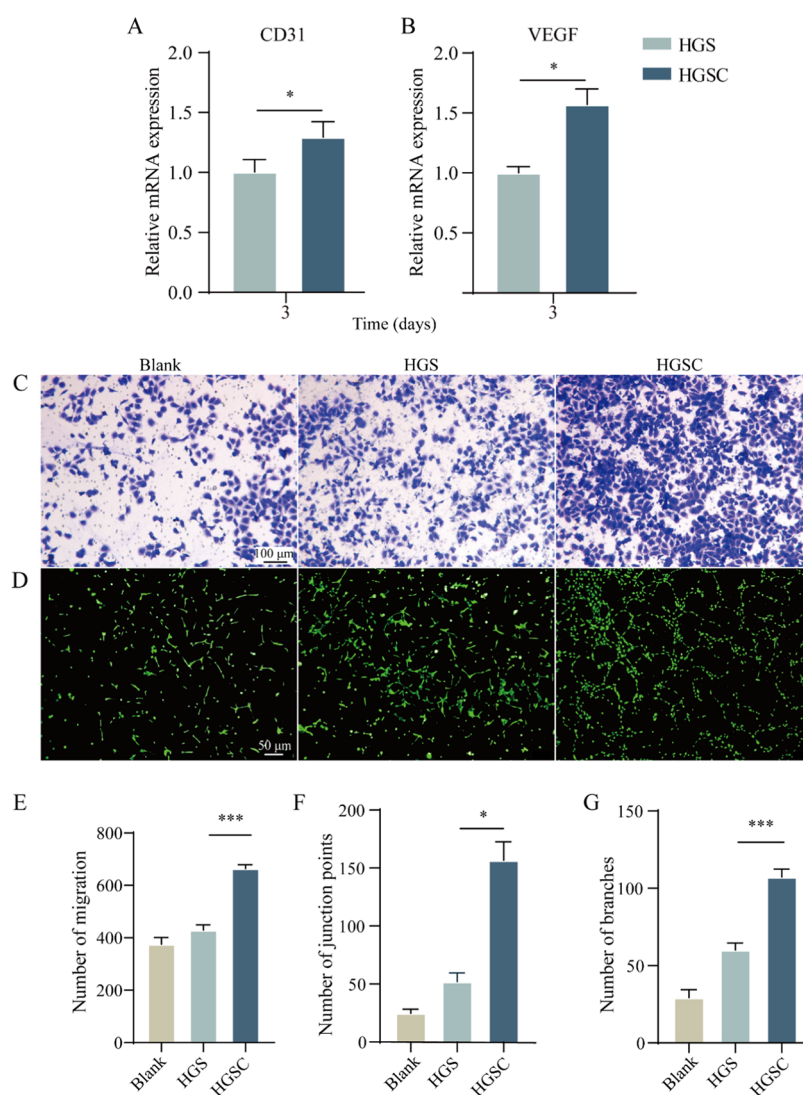


Figure 5. Evaluation of HGS/HGSC composite scaffold-induced vascularization of HUVECs in vitro. (A) CD31 mRNA expression; (B) VEGF mRNA expression; (C) representative images of the transwell assay and quantified as (E) number of migration; (D) tubular formation assay of HUVECs after culturing with extracts and quantified as (F) number of junction points; and (G) number of branches (* $P < 0.05$, *** $P < 0.001$, $n = 3$).

stress–strain curve showed that the HGSC scaffold had lower variability than the HGS scaffold (Figure 3F).

3.6. Cell Adhesion. In this study, BMSCs were able to adhere well to the scaffolds and maintained their cellular morphology, indicating the good biocompatibility of the HGS/HGSC scaffolds (Figure 4A).

3.7. Evaluation of Scaffold Toxicity and Proliferation Characteristics. In this study, there were no significant differences in cell viability among the groups on days 1 and 3. However, by day 7, the HGSC group exhibited significantly higher cell proliferation than the HGS group (Figure 4B). Results from live/dead fluorescence staining showed that in both groups, the majority of cells emitted green fluorescence, indicating live cells, while only a small number of cells emitted red fluorescence, indicating dead cells. This suggests that the scaffold is nontoxic (Figure 4C). The EdU results further confirmed our initial hypothesis, indicating that the HGSC scaffold possesses excellent biocompatibility and nontoxicity, making it suitable for continued use in subsequent cell experiments (Figure 4D).

3.8. In Vitro Effect of Scaffolds on Angiogenesis in HUVECs. After coculturing SE and HUVECs for 3 days, the expression of the gene markers CD31 and VEGF was detected by RT-qPCR (Figure 5A,B). The experimental results showed significantly upregulated gene expression related to angiogenesis in the experimental group compared to the control group. The results of the transwell experiment showed that the number of HUVECs migrating was significantly higher than that of the control group and was quantitatively analyzed (Figure 5C,E). The tube formation assay demonstrated significant tube-like structure formation on the HGSC scaffold (Figure 5D). Quantitative analysis of the number of nodes and branches significantly differed between the groups (Figure 5F,G).

3.9. In Vitro Effect of the Scaffold on the Osteogenic Differentiation of BMSCs. Following 3 and 7 days of culture, we conducted RT-qPCR to assess the expression of osteogenic markers ALP and OCN (osteocalcin). The results indicated that the expression of these markers increased with the duration of culture, and by the seventh day, the HGSC scaffold group exhibited significantly higher expression levels compared to the HGS group (Figure 6A,B). These findings suggest that the

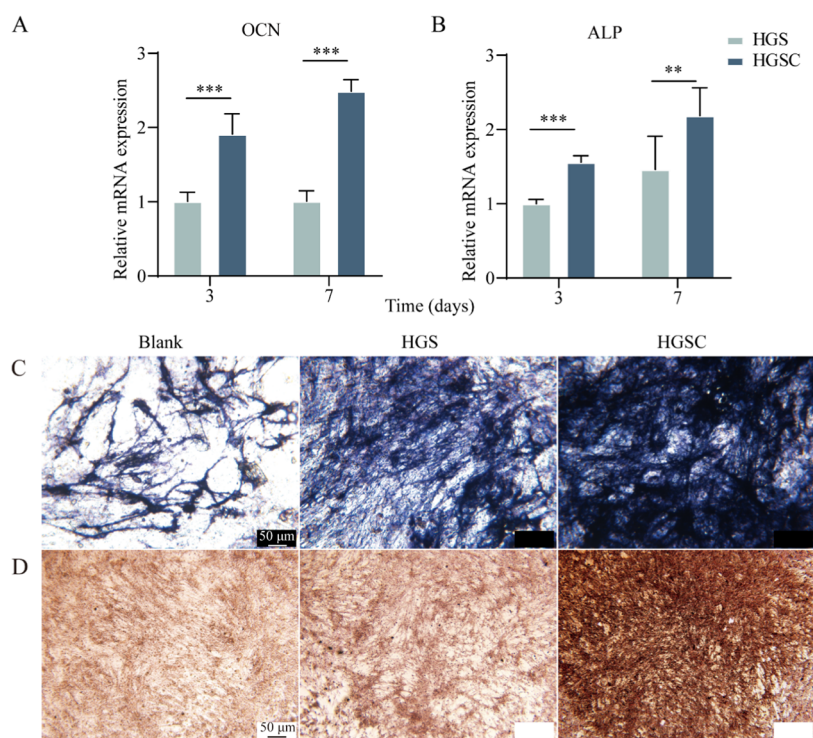


Figure 6. Evaluation of osteogenic differentiation of BMSCs induced by HGS/HGSC composite scaffolds in vitro. (A, B) Osteogenesis-related gene expression on days 3 and 7 (A) OCN, (B) ALP, (** $P < 0.01$ and *** $P < 0.001$, $n = 3$); (C, D) alkaline phosphatase and Alizarin Red staining in coculture of SE with BMSC.

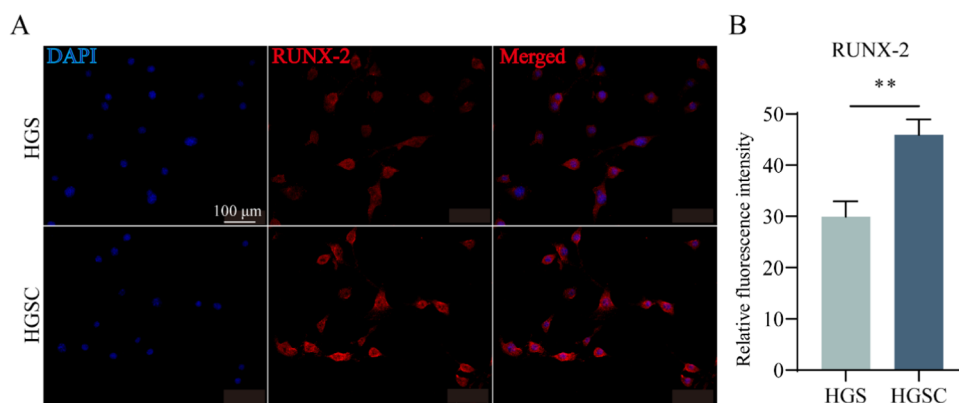


Figure 7. (A) RUNX2 cell immunofluorescence staining on Scaffolds; (B) quantitative analysis of RUNX2 fluorescence intensity (** $P < 0.01$, $n = 3$).

HGSC composite scaffold may have a positive role in inducing osteogenic differentiation. Alkaline phosphatase (ALP) is considered an early osteogenic marker.²⁵ Our research results demonstrate that the HGSC group exhibits higher ALP activity compared to the HGS group, confirming its enhanced osteogenic potential (Figure 6D). Additionally, we conducted Alizarin Red S staining (ARS), a late-stage osteogenic marker, which further validated the abundant formation of mineralized nodules within the HGSC scaffold during the later stages of culture (Figure 6C). In addition to ALP analysis, we also conducted immunofluorescence staining for another early osteogenic marker, RUNX2, and quantitatively analyzed the fluorescence intensity. Similar to the ALP and ARS results, the fluorescence intensity in the HGSC group was significantly higher than that in the HGS group, providing additional support for the concept of enhanced osteogenic characteristics within the HGSC scaffold (Figure 7A,B).

4.0. WESTERN BLOTTING ASSAY

Using immunoblotting, we monitored the levels of proteins associated with angiogenesis and osteogenesis. The results (Figure 8A,B) indicate a significant increase in the levels of angiogenesis-related proteins HIF-1 α and VEGF, as well as osteogenesis-related proteins RUNX2 and Osterix in the HGSC scaffold compared to the control group. Quantitative analysis of the grayscale values of the protein expressions was performed (Figure 8C,D).

4.1. Micro-CT Scanning Analysis. After 8 weeks post-operatively, observation of rat skull using Micro-CT scanning revealed mild bone filling in the blank control group and the HGS group, while the HGSC group exhibited significantly superior new bone repair compared to the other two groups (Figure 9A). Analysis showed that the bone volume fraction in the HGSC group was significantly higher than the control group, reaching 1.9–2.1 times, with significant statistical significance

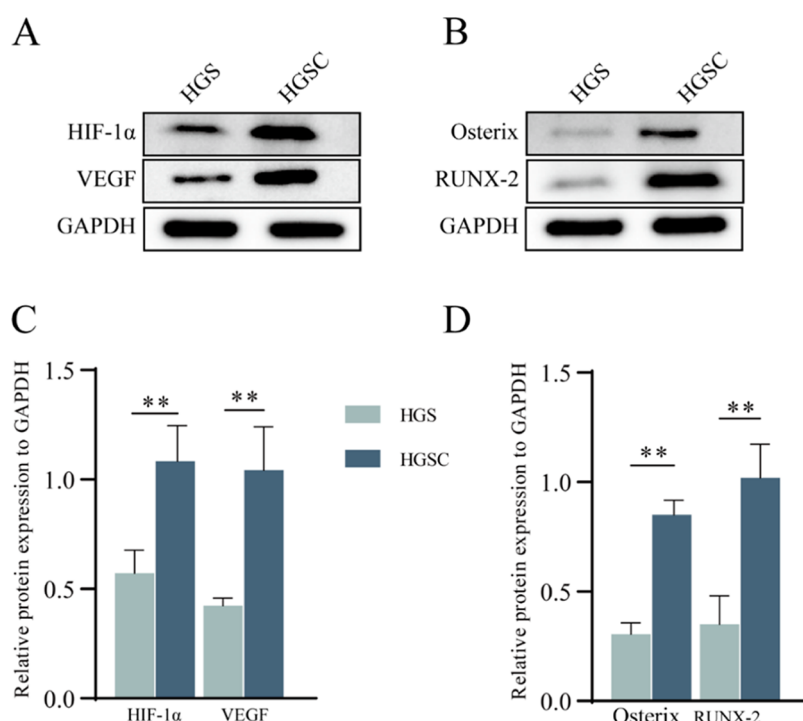


Figure 8. Expression of vascular and osteogenic-related proteins in scaffolds. (A) Expression diagram of angiogenesis-related proteins HIF-1 α and VEGF in scaffolds cultured with HUVECs for 3 days; (B) expression diagram of osteogenesis-related proteins RUNX2 and Osterix in scaffolds cultured with BMSCs for 7 days; (C) quantitative analysis of HIF-1 α and VEGF expression relative to GAPDH; and (D) quantitative analysis of RUNX2 and Osterix expression relative to GAPDH (** $P < 0.01$, $n = 3$).

(Figure 9B). The cross-sectional trabecular number in the HGSC group showed a significant increase, reaching 1.6–1.8 times, also with significant statistical significance (Figure 9C). This indicates a significant advantage of HGSC in new bone generation.

4.2. H&E Staining and Masson's Staining Results. To assess the impact of the scaffold on osteoinduction and vascular generation, we conducted H&E staining and Masson's staining. In H&E staining, we observed scattered network-like blood vessels near the scaffold, and all groups showed varying degrees of new bone formation. However, the bone matrix in the HGSC group was significantly higher than in the other two groups. Similarly, Masson's staining results also showed that in the blank and control groups, only a small amount of bone collagen and bone matrix was present, while in the HGSC group, a large amount of new bone and mature bone tissue filled the bone defect site (Figure 10A,B). These results are consistent with the Micro-CT findings, further highlighting the significant effect of the HGSC scaffold in promoting bone integration.

4.3. Immunofluorescence Staining of Tissues. As is well known, the generation of blood vessels can greatly impact local new bone formation. We used immunofluorescence staining to evaluate the expression of the new vascular marker CD31 at the calvarial defect site (Figure 11A,B). We found that 8 weeks postsurgery, the positivity rate in the HGSC group was significantly higher than in the HGS group and the blank group. We also conducted a quantitative analysis of fluorescence intensity, indicating that the HGSC scaffold can effectively promote vascular generation at the calvarial defect site, effectively synergizing with new bone formation.

5. DISCUSSION

In the context of bone tissue engineering, despite significant advancements in three-dimensional drug delivery scaffolds for their high precision and personalized medication, challenges such as high side effects, burst drug release, and low drug utilization cannot be overlooked.²⁶ Although some studies suggest that chemical reactions or scaffold degradation can mitigate the sudden release of drugs, concerns about low drug utilization persist.²⁷ The widespread application of PCL microsphere drug delivery systems addresses many shortcomings compared to traditional scaffolds, including poor biological activity and drug release associated with drug incorporation or coating.²⁸ The PCL microsphere drug delivery system not only enhances the biological activity of the scaffold but also facilitates controlled drug release, playing a crucial role in targeted drug delivery and improving biocompatibility.²⁹ Curculigoside (CUR) is a natural phenol glycoside compound extracted from *Curculigo orchoides*, which promotes osteogenic differentiation of adipose-derived stem cells (ADSCs) by activating the PI3K/Akt signaling pathway. Researchers have also found that CUR significantly promotes the phosphorylation of AKT, thereby converting it into P-AKT, which is essential for the osteogenic differentiation process.³⁰ Wang et al. reported that CUR can enhance the expression of transcriptional coactivator with PDZ-binding motif (TAZ), thereby increasing osteogenic activity in BMSCs.³¹ According to Chengjian Ma et al., MC3T3-E1 cells treated with CUR showed significantly upregulated protein expression of VEGF and BMP-2.²⁰ These findings are consistent with the conclusions obtained from in vitro and in vivo experiments. They provide reliable evidence for the osteogenic-promoting properties of the prepared HGSC scaffold. It has been reported that the scaffold exhibits angiogenic and osteogenic effects by incorporating various

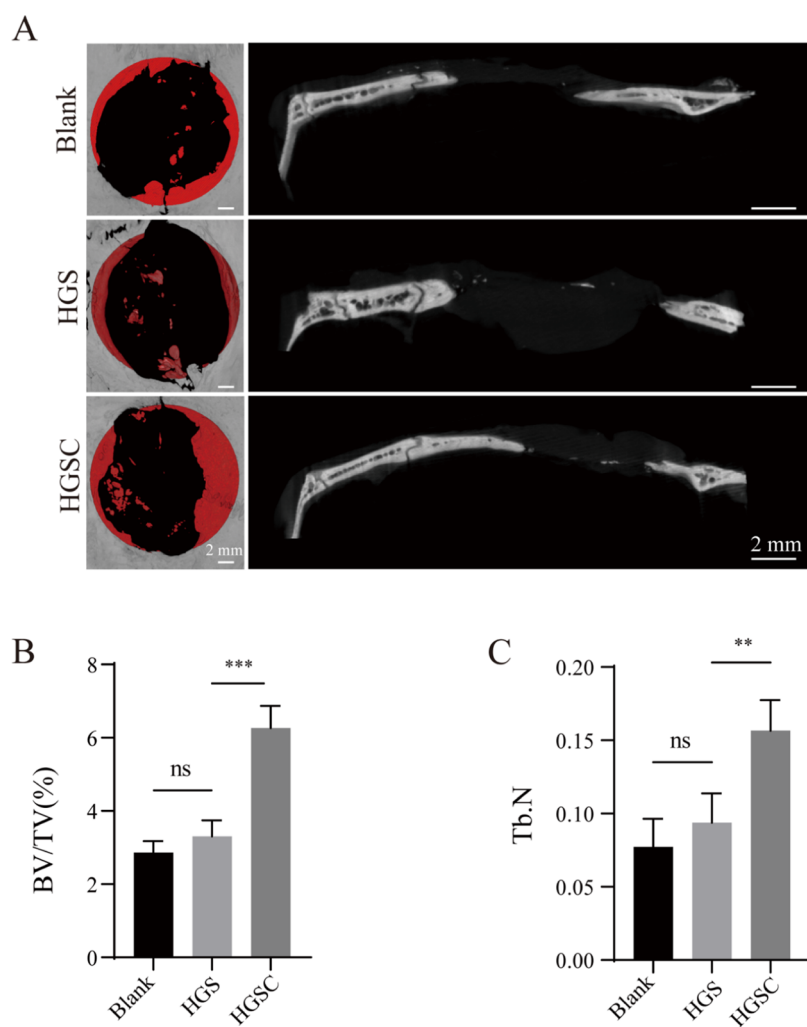


Figure 9. Rat calvarial defects with scaffold-induced new bone regeneration at 8 weeks postsurgery. (A) Micro-CT scan images; (B) and (C) quantitative analyses of bone volume and cross-sectional trabecular number (** $P < 0.01$, $n = 3$).

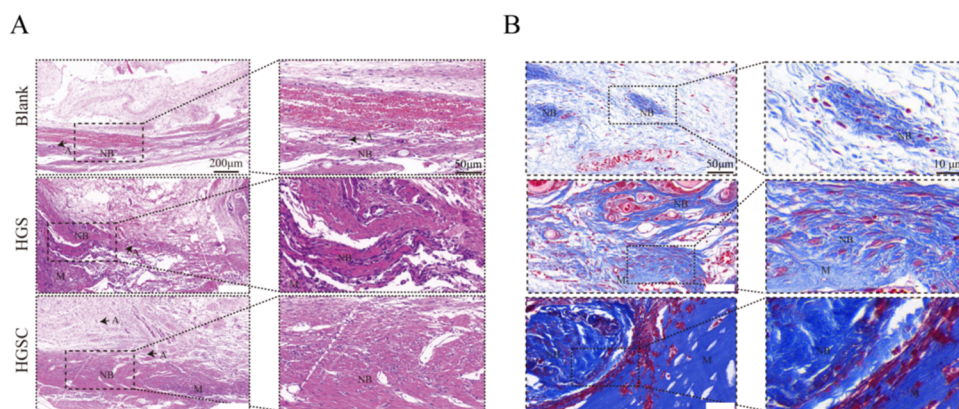


Figure 10. Histological staining evaluation of bone regeneration at 8 weeks postsurgery. (A) H&E staining images; (B) Masson's trichrome staining images (A = angiogenesis, NB = new bone, and M = composite scaffold).

growth factors, but their preparation process is prone to inactivation.³² Compared to electrospray, solution casting, and gel particle formation methods for microsphere preparation, the emulsion/solvent evaporation method stands out for its simplicity, cost-effectiveness, and suitability for hydrophobic drugs.^{33–35} To this end, we successfully prepared CUR@PM nanomicrospheres with a size of approximately 15.7 ± 14 nm

using the emulsion/solvent evaporation method. These nanomicrospheres, integrated with 3D printing technology, were employed to construct an HGSC (hydroxyapatite/gelatin/sodium alginate) scaffold.

The excellent rheological properties of the bioink are foundational for the successful fabrication of 3D-printed scaffolds. Both groups of scaffolds exhibited good stability and

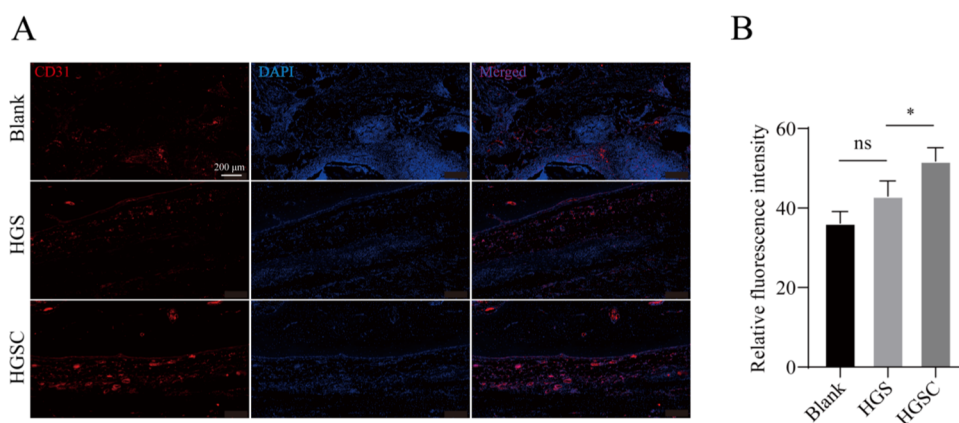


Figure 11. Immunofluorescence expression related to vascularization in bone defect tissues. (A) CD31 fluorescence expression images at the calvarial defect site 8 weeks postsurgery; (B) quantitative analysis of CD31 fluorescence intensity (* $P < 0.05$, $n = 3$).

shear-thinning behavior in their bioink, ensuring that the materials could maintain stable flowability and shape flexibility during the printing process.³⁶ Despite the hydrophobic nature of the nanomicrospheres, they constitute a small proportion of the HGSC scaffold, resulting in no significant difference in water absorption between the two scaffold groups. Concerning drug release over time, the nanomicrospheres exhibited a faster drug release rate. This difference reflects the secondary encapsulation of the drug microspheres within the scaffold, significantly slowing drug release. This sustained drug release capability addresses a primary concern in drug delivery, allowing for long-term regulation of local drug concentrations and higher drug efficacy without adverse side effects. The drug loading results of the nanomicrospheres suggest that the PM designed by us has the capacity to effectively load curculigoside. In both cell culture and animal implantation, biocompatible and nontoxic scaffolds are essential for facilitating normal cell proliferation and differentiation. Subsequent experiments, including CCK-8, cell adhesion, and EdU assays, successfully validated the biocompatibility of the HGSC scaffold, laying the foundation for further research.^{37,38} New blood vessel formation is essential for bone regeneration, development, and remodeling.³⁹ Endothelial cell migration assays and tube formation assays are common methods for evaluating the angiogenic potential of *in vitro* studies. Our results indicate that after stimulation with conditioned medium from HGSC scaffolds, there is significant directional chemotaxis and angiogenic potential. Additionally, we found that HGSC scaffolds can upregulate the expression of genes related to angiogenesis and increase the expression of HIF-1 α and VEGF proteins. This is because abnormal activation of the HIF-1 α signaling pathway stimulates the upregulation of VEGF expression, thereby promoting angiogenesis.⁴⁰ Therefore, we believe that encapsulating curculigoside can stimulate the transcriptional activity of HIF-1 α and promote VEGF expression, thereby enabling the composite scaffold to promote the vascularization and migratory capacity of HUVECs. Youlu Chen and others have pointed out that vascular regeneration can be achieved in a mouse model by directly encapsulating the VEGF gene.⁴¹ Osteoblast differentiation is a prerequisite for bone regeneration.⁴² Therefore, we conducted osteogenic gene detection analysis, alkaline phosphatase staining (ALP), Alizarin Red staining (ARS), and western blot experiments for each group. ALP and OCN are widely recognized as specific indicators of osteogenic differentiation. By detecting the expression levels of bone genes, the results show that the

composite scaffold loaded with CUR@PM exhibits high expression of OCN and ALP. We believe this may be due to the combination of hydroxyapatite and CUR@PM, which helps enhance the osteogenic gene expression ability of BMSCs. ALP is an early marker of osteogenic differentiation and plays an important role in the conversion of inorganic pyrophosphate to inorganic phosphate during mineralization.⁴³ ARS staining is an important marker of late-stage mineralized bone nodules, and the experimental results show strong positivity after culturing with HGSC and BMSCs.⁴⁴ This is consistent with Wu et al.'s method of verifying osteogenic potential by using electrospinning technology to load telmisartan and promote osteogenesis through macrophage M2 polarization.³⁸ Furthermore, we conducted western blot experiments, where RUNX2 and Osterix are key transcription factors regulating early osteogenesis and late-stage bone mineralization, respectively.⁴⁵ Our *in vitro* results are similar to those reported in the existing literature.²⁰ In summary, we can reasonably conclude that HGSC scaffolds possess angiogenic and enhanced osteogenic functions. Previous literature has indicated that the generation of Osterix is regulated by RUNX2, and Osterix, in turn, influences the downstream processes of RUNX2, involving various aspects of bone formation.⁴⁶ In subsequent studies, we intend to delve into the specific molecular mechanisms between these molecules, further elucidating their collaborative regulatory mechanisms in the process of bone formation.

In order to directly observe the new bone growth at the defect sites of each group, we utilized Micro-CT for evaluation. Biocompatibility and nontoxicity are prerequisites for materials implanted *in vivo*, while possessing degradation capability is also essential.⁴⁷ According to the imaging results, we found varying degrees of new bone ingrowth at the defect sites, indicating that our composite scaffold exhibits excellent biocompatibility and nontoxicity while also possessing appropriate degradation characteristics. This finding is consistent with the conclusion of Ma et al., who reported that a composite scaffold constructed by combining hydroxyapatite with nanoattapulgitite (ATP) promotes rabbit tibial defect repair.¹⁴ This characteristic facilitates gradual degradation of the scaffold after implantation into the bone defect, gradually replaced by new bone tissue, thereby providing rapid healing while also contributing to the restoration of the natural biomechanical properties of bone tissue. Trabeculae are structures that extend from cortical bone to cancellous bone, primarily providing support within the bone marrow cavity. In addition to qualitative analysis by micro-CT,

we also conducted quantitative analysis of bone volume fraction and trabecular parameters. According to the literature, tumor diseases promote bone metabolism, thereby exacerbating osteoporosis.⁴⁸ The results at 8 weeks postoperatively showed that both bone volume fraction and trabecular parameters were significantly higher in the HGSC group compared to the HGS scaffold. This indicates the HGSC group exhibited features of new bone formation and abundant mature bone tissue.⁴⁹ HE staining results revealed a large amount of connective tissue ingrowth in the Blank group and HGS group, along with a small amount of new bone formation, as well as a small number of neovascularization. In the HGSC group, there was a significant irregular bone formation. Masson's staining was used to stain collagen fibers, further evaluating bone formation and maturity. This further confirmed the role of HGSC in promoting new bone tissue generation. These findings are consistent with the results of Micro-CT scanning analysis. CD31 is a cell adhesion molecule involved in angiogenesis or neovascularization. We assessed the vascularization of the scaffold at the defect site through CD31 immunofluorescence, which is consistent with the method our research team previously validated for assessing vascularization.⁵⁰ In conclusion, we believe that the vascularization performance and superior bone regeneration of the HGSC scaffold may be attributed to the sustained release of CUR@PM postimplantation and the intrinsic osteoinductive properties of hydroxyapatite itself, thereby maximizing bone integration.

6. CONCLUSIONS

Based on the research results, HGSC exhibits excellent physicochemical properties. Importantly, it can slowly and continuously release CUR, enhancing drug utilization and safety, thereby demonstrating its nontoxicity and biocompatibility. Through the analysis of osteogenic gene and cell protein expression, as well as micro-CT and tissue staining results, we have validated the outstanding performance of the scaffold in promoting osteogenesis and vascular formation. Therefore, our research results suggest that this CUR-loaded composite scaffold significantly strengthens the osteogenic effect of the scaffold, providing strong support for its application in the field of bone tissue engineering.

■ ASSOCIATED CONTENT

Data Availability Statement

All data relevant to the study are included in the article.

■ AUTHOR INFORMATION

Corresponding Authors

Yifei Shen – *The Affiliated Changzhou Second People's Hospital of Nanjing Medical University, Changzhou Medical Center, Nanjing Medical University, Changzhou 213003, China*; orcid.org/0000-0002-1401-7183; Email: nydshenyifei@163.com

Zhonghua Zhang – *Changzhou Economic Development District Hengshanqiao People's Hospital, Changzhou 213003, China*; Email: 2235266132@qq.com

Hua Xu – *State Key Laboratory of Bioelectronics, School of Biological Science and Medical Engineering, Southeast University, Nanjing 210096, China*; orcid.org/0000-0002-5398-0044; Email: huaxu@seu.edu.cn

Authors

Yiping Weng – *State Key Laboratory of Bioelectronics, School of Biological Science and Medical Engineering, Southeast*

University, Nanjing 210096, China; Graduate School of Bengbu Medical College, Bengbu 233030, China
Xiuchen Yuan – *Graduate School of Bengbu Medical College, Bengbu 233030, China*
Shijie Fan – *The Affiliated Changzhou Second People's Hospital of Nanjing Medical University, Changzhou Medical Center, Nanjing Medical University, Changzhou 213003, China*
Weihao Duan – *The Affiliated Changzhou Second People's Hospital of Nanjing Medical University, Changzhou Medical Center, Nanjing Medical University, Changzhou 213003, China*
Yadong Tan – *The Affiliated Changzhou Second People's Hospital of Nanjing Medical University, Changzhou Medical Center, Nanjing Medical University, Changzhou 213003, China*
Ruikai Zhou – *The Affiliated Changzhou Second People's Hospital of Nanjing Medical University, Changzhou Medical Center, Nanjing Medical University, Changzhou 213003, China*
Jingbin Wu – *The Affiliated Changzhou Second People's Hospital of Nanjing Medical University, Changzhou Medical Center, Nanjing Medical University, Changzhou 213003, China*

Complete contact information is available at:

<https://pubs.acs.org/10.1021/acsomega.4c01533>

Author Contributions

Y.W. and X.Y. have contributed equally to this work and shared the first authorship. Y.W.: Writing—original draft. H.X. and Y.S.: Conceptualization, supervision, and writing—review and editing. S.F.: Resources. W.D.: Resources and conceptualization. Y.T. and Z.Z.: Resources. R.Z.: Resources. J.W.: Resources.

Funding

The Changzhou Science and Technology Program (CE20215020 and CQ20220113), the Changzhou Medical Center of Nanjing Medical University Project (CMCC202217), and the Youth Fund of the Changzhou Municipal Health and Family Planning Commission (QN202365).

Notes

The authors declare no competing financial interest.

■ ACKNOWLEDGMENTS

This study was supported by the Changzhou Sci&Tech Program (CE20215020) and Subject of Changzhou Medical Center of Nanjing Medical University (CMCC202217).

■ REFERENCES

- (1) Lauer, A.; Wolf, P.; Mehler, D.; Gotz, H.; Ruzgar, M.; Baranowski, A.; Henrich, D.; Rommens, P. M.; Ritz, U. Biofabrication of SDF-1 Functionalized 3D-Printed Cell-Free Scaffolds for Bone Tissue Regeneration. *Int. J. Mol. Sci.* **2020**, *21* (6), 2175.
- (2) Liu, C.; Qin, W.; Wang, Y.; Ma, J.; Liu, J.; Wu, S.; Zhao, H. 3D Printed Gelatin/Sodium Alginate Hydrogel Scaffolds Doped with Nano-Attapulgite for Bone Tissue Repair. *Int. J. Nanomed.* **2021**, *16*, 8417–8432.
- (3) Ying, C.; Wang, R.; Wang, Z.; Tao, J.; Yin, W.; Zhang, J.; Yi, C.; Qi, X.; Han, D. BMSC-Exosomes Carry Mutant HIF-1 α for Improving Angiogenesis and Osteogenesis in Critical-Sized Calvarial Defects. *Front. Bioeng. Biotechnol.* **2020**, *8*, No. 565561.
- (4) Mistry, S.; Burman, S.; Roy, S.; Maitra, N. J.; Roy, R.; Chanda, A. Biological analysis of an innovative biodegradable antibiotic eluting bioactive glass/gypsum composite bone cement for treating exper-

- imental chronic MRSA osteomyelitis. *J. Pharm. Anal.* **2022**, *12* (1), 164–177.
- (5) Yuan, Y.; Chen, L.; Shi, Z.; Chen, J. Micro/Nanoarchitectonics of 3D Printed Scaffolds with Excellent Biocompatibility Prepared Using Femtosecond Laser Two-Photon Polymerization for Tissue Engineering Applications. *Nanomaterials* **2022**, *12* (3), 391.
- (6) Dang, M.; Saunders, L.; Niu, X.; Fan, Y.; Ma, P. X. Biomimetic delivery of signals for bone tissue engineering. *Bone Res.* **2018**, *6*, 25.
- (7) Billings, C.; Bow, A. J.; Newby, S. D.; Donnell, R. L.; Dhar, M.; Anderson, D. E. Effects on Tissue Integration of Collagen Scaffolds Used for Local Delivery of Gentamicin in a Rat Mandible Defect Model. *Bioengineering* **2022**, *9* (7), 275.
- (8) Qi, C.; Deng, Y.; Xu, L.; Yang, C.; Zhu, Y.; Wang, G.; Wang, Z.; Wang, L. A sericin/graphene oxide composite scaffold as a biomimetic extracellular matrix for structural and functional repair of calvarial bone. *Theranostics* **2020**, *10* (2), 741–756.
- (9) Li, J.; Wei, J.; Li, A.; Liu, H.; Sun, J.; Qiao, H. A Dual Peptide Sustained-Release System Based on Nanohydroxyapatite/Polyamide 66 Scaffold for Synergistic-Enhancing Diabetic Rats' Fracture Healing in Osteogenesis and Angiogenesis. *Front. Bioeng. Biotechnol.* **2021**, *9*, No. 657699.
- (10) Xu, D.; Gan, K.; Wang, Y.; Wu, Z.; Wang, Y.; Zhang, S.; Peng, Y.; Fang, X.; Wei, H.; Zhang, Y.; et al. A Composite Deferoxamine/Black Phosphorus Nanosheet/Gelatin Hydrogel Scaffold for Ischemic Tibial Bone Repair. *Int. J. Nanomed.* **2022**, *17*, 1015–1030.
- (11) Servat-Medina, L.; Gonzalez-Gomez, A.; Reyes-Ortega, F.; Sousa, I. M.; Queiroz Nde, C.; Zago, P. M.; Jorge, M. P.; Monteiro, K. M.; de Carvalho, J. E.; San Roman, J.; Foglio, M. A. Chitosan-tripolyphosphate nanoparticles as *Arrabidaea chica* standardized extract carrier: synthesis, characterization, biocompatibility, and antiulcerogenic activity. *Int. J. Nanomed.* **2015**, *10*, 3897–3909.
- (12) Paolini, A.; Battafarano, G.; D'Oria, V.; Mura, F.; Sennato, S.; Mussi, V.; Risoluti, R.; Materazzi, S.; Del Fattore, A.; Masotti, A. A 3D-Printed Multi-Chamber Device Allows Culturing Cells On Bucky-papers Coated With PAMAM Dendrimer And Obtain Innovative Materials For Biomedical Applications. *Int. J. Nanomed.* **2019**, *14*, 9295–9306.
- (13) Wang, H.; Hu, B.; Li, H.; Feng, G.; Pan, S.; Chen, Z.; Li, B.; Song, J. Biomimetic Mineralized Hydroxyapatite Nanofiber-Incorporated Methacrylated Gelatin Hydrogel with Improved Mechanical and Osteoinductive Performances for Bone Regeneration. *Int. J. Nanomed.* **2022**, *17*, 1511–1529.
- (14) Ma, J.; Wu, S.; Liu, J.; Liu, C.; Ni, S.; Dai, T.; Wu, X.; Zhang, Z.; Qu, J.; Zhao, H.; et al. Synergistic effects of nanoattapulgitic and hydroxyapatite on vascularization and bone formation in a rabbit tibia bone defect model. *Biomater. Sci.* **2022**, *10* (16), 4635–4655.
- (15) Dubbin, K.; Tabet, A.; Heilshorn, S. C. Quantitative criteria to benchmark new and existing bio-inks for cell compatibility. *Biofabrication* **2017**, *9* (4), No. 044102.
- (16) Lee, H. P.; Alisafaei, F.; Adebawale, K.; Chang, J.; Shenoy, V. B.; Chaudhuri, O. The nuclear piston activates mechanosensitive ion channels to generate cell migration paths in confining microenvironments. *Sci. Adv.* **2021**, *7* (2), No. eabd4058, DOI: 10.1126/sciadv.abd4058.
- (17) Liu, J.; Wu, S.; Ma, J.; Liu, C.; Dai, T.; Wu, X.; Zhao, H.; Zhou, D. Polycaprolactone/Gelatin/Hydroxyapatite Electrospun Nanomembrane Materials Incorporated with Different Proportions of Attapulgitic Synergistically Promote Bone Formation. *Int. J. Nanomed.* **2022**, *17*, 4087–4103.
- (18) Tian, X.; Yuan, X.; Feng, D.; Wu, M.; Yuan, Y.; Ma, C.; Xie, D.; Guo, J.; Liu, C.; Lu, Z. In vivo study of polyurethane and tannin-modified hydroxyapatite composites for calvarial regeneration. *J. Tissue Eng.* **2020**, *11*, No. 2041731420968030.
- (19) Sancilio, S.; Marsich, E.; Schweikl, H.; Cataldi, A.; Gallorini, M. Redox Control of IL-6-Mediated Dental Pulp Stem-Cell Differentiation on Alginate/Hydroxyapatite Biocomposites for Bone Ingrowth. *Nanomaterials* **2019**, *9* (12), 1656.
- (20) Ma, C.; Zhang, J.; Fu, J.; Cheng, L.; Zhao, G.; Gu, Y. Up-regulation of VEGF by MC3T3-E1 cells treated with curculigoside. *Phytother. Res.* **2011**, *25* (6), 922–926.
- (21) Tan, Y.; Fan, S.; Wu, X.; Liu, M.; Dai, T.; Liu, C.; Ni, S.; Wang, J.; Yuan, X.; Zhao, H.; Weng, Y. Fabrication of a three-dimensional printed gelatin/sodium alginate/nano-attapulgitic composite polymer scaffold loaded with leonurine hydrochloride and its effects on osteogenesis and vascularization. *Int. J. Biol. Macromol.* **2023**, *249*, No. 126028.
- (22) Norouzi, M. R.; Ghasemi-Mobarakeh, L.; Itef, F.; Schoeller, J.; Fashandi, H.; Borzi, A.; Neels, A.; Fortunato, G.; Rossi, R. M. Emulsion electrospinning of sodium alginate/poly(epsilon-caprolactone) core/shell nanofibers for biomedical applications. *Nanoscale Adv.* **2022**, *4* (13), 2929–2941.
- (23) Lu, B.; Han, X.; Zhao, A.; Luo, D.; Maitz, M. F.; Wang, H.; Yang, P.; Huang, N. Intelligent H2S release coating for regulating vascular remodeling. *Bioact. Mater.* **2021**, *6* (4), 1040–1050.
- (24) Fang, C. H.; Lin, Y. W.; Lin, F. H.; Sun, J. S.; Chao, Y. H.; Lin, H. Y.; Chang, Z. C. Biomimetic Synthesis of Nanocrystalline Hydroxyapatite Composites: Therapeutic Potential and Effects on Bone Regeneration. *Int. J. Mol. Sci.* **2019**, *20* (23), 6002.
- (25) Maređziak, M.; Smieszek, A.; Chrzastek, K.; Basinska, K.; Marycz, K. Physical Activity Increases the Total Number of Bone-Marrow-Derived Mesenchymal Stem Cells, Enhances Their Osteogenic Potential, and Inhibits Their Adipogenic Properties. *Stem Cells Int.* **2015**, *2015*, No. 379093.
- (26) Lu, S.; Zhao, F.; Zhang, Q.; Chen, P. Therapeutic Peptide Amphiphile as a Drug Carrier with ATP-Triggered Release for Synergistic Effect, Improved Therapeutic Index, and Penetration of 3D Cancer Cell Spheroids. *Int. J. Mol. Sci.* **2018**, *19* (9), 2773.
- (27) Yuan, F. Z.; Wang, H. F.; Guan, J.; Fu, J. N.; Yang, M.; Zhang, J. Y.; Chen, Y. R.; Wang, X.; Yu, J. K. Fabrication of Injectable Chitosan-Chondroitin Sulfate Hydrogel Embedding Kartogenin-Loaded Microspheres as an Ultrasound-Triggered Drug Delivery System for Cartilage Tissue Engineering. *Pharmaceutics* **2021**, *13* (9), 1487.
- (28) Xie, Y.; Sun, W.; Yan, F.; Liu, H.; Deng, Z.; Cai, L. Icarin-loaded porous scaffolds for bone regeneration through the regulation of the coupling process of osteogenesis and osteoclastic activity. *Int. J. Nanomed.* **2019**, *14*, 6019–6033.
- (29) Banstola, A.; Pham, T. T.; Jeong, J. H.; Yook, S. Polydopamine-tailored paclitaxel-loaded polymeric microspheres with adhered NIR-controllable gold nanoparticles for chemo-phototherapy of pancreatic cancer. *Drug Delivery* **2019**, *26* (1), 629–640.
- (30) You, W. L.; Xu, Z. L. Curculigoside promotes osteogenic differentiation of ADSCs to prevent ovarietomized-induced osteoporosis. *J. Orthop. Surg. Res.* **2021**, *16* (1), 279.
- (31) Wang, N.; Li, Z.; Li, S.; Li, Y.; Gao, L.; Bao, X.; Wang, K.; Liu, C.; Xue, P.; Liu, S. Curculigoside Ameliorates Bone Loss by Influencing Mesenchymal Stem Cell Fate in Aging Mice. *Front. Cell Dev. Biol.* **2021**, *9*, No. 767006.
- (32) Kong, D.; Shi, Y.; Gao, Y.; Fu, M.; Kong, S.; Lin, G. Preparation of BMP-2 loaded MPEG-PCL microspheres and evaluation of their bone repair properties. *Biomed. Pharmacother.* **2020**, *130*, No. 110516.
- (33) Wang, H.; Hu, H.; Zhang, X.; Zheng, L.; Ruan, J.; Cao, J.; Zhang, X. Preparation, Physicochemical Characterization, and Antioxidant Activity of Naringin-Silk Fibroin-Alginate Microspheres and Application in Yogurt. *Foods* **2022**, *11* (14), 2147.
- (34) Ren, Q.; Wu, G.; Xing, W.; Han, J.; Li, P.; Li, B.; Cheng, J.; Wu, S.; Zou, R.; Hu, J. Highly Ordered Mesoporous NiCo(2)O(4) as a High Performance Anode Material for Li-Ion Batteries. *Front. Chem.* **2019**, *7*, 521.
- (35) Wu, Z.; Yang, H.; Tian, F.; Ren, H.; Chen, Y. Effective Tuning of the Performance of Conductive Silicon Compound by Few-Layered Graphene Additives. *Nanomaterials* **2022**, *12* (6), 907.
- (36) Liu, C.; Dai, T.; Wu, X.; Ma, J.; Liu, J.; Wu, S.; Yang, L.; Zhao, H. 3D bioprinting of cell-laden nano-attapulgitic/gelatin methacrylate composite hydrogel scaffolds for bone tissue repair. *J. Mater. Sci. Technol.* **2023**, *135*, 111–125.
- (37) Ji, Q.; Wang, Z.; Jiao, Z.; Wang, Y.; Wu, Z.; Wang, P.; Zhu, Y.; Sun, S.; Liu, Y.; Zhang, P. Biomimetic polyetheretherketone micro-

carriers with specific surface topography and self-secreted extracellular matrix for large-scale cell expansion. *Regener. Biomater.* **2019**, *7* (1), 109–118.

(38) Wu, S.; Ma, J.; Liu, J.; Liu, C.; Ni, S.; Dai, T.; Wang, Y.; Weng, Y.; Zhao, H.; Zhou, D.; Zhao, X. Immunomodulation of Telmisartan-Loaded PCL/PVP Scaffolds on Macrophages Promotes Endogenous Bone Regeneration. *ACS Appl. Mater. Interfaces* **2022**, *14* (14), 15942–15955.

(39) Gandolfi, M. G.; Zamparini, F.; Valente, S.; Parchi, G.; Pasquinelli, G.; Taddei, P.; Prati, C. Green Hydrogels Composed of Sodium Mannuronate/Guluronate, Gelatin and Biointeractive Calcium Silicates/Dicalcium Phosphate Dihydrate Designed for Oral Bone Defects Regeneration. *Nanomaterials* **2021**, *11* (12), 3439.

(40) Foglietta, F.; Gola, G.; Biasibetti, E.; Capucchio, M. T.; Bruni, I.; Francovich, A.; Durando, G.; Serpe, L.; Canaparo, R. 5-Aminolevulinic Acid Triggered by Ultrasound Halts Tumor Proliferation in a Syngeneic Model of Breast Cancer. *Pharmaceuticals* **2021**, *14* (10), 972.

(41) Chen, Y.; Chen, Z.; Duan, J.; Gui, L.; Li, H.; Liang, X.; Tian, X.; Liu, K.; Li, Y.; Yang, J. H(2)O(2)-responsive VEGF/NGF gene co-delivery nano-system achieves stable vascularization in ischemic hindlimbs. *J. Nanobiotechnology* **2022**, *20* (1), 145.

(42) Feric, N. T.; Cheng, C. C.; Goh, M. C.; Dudnyk, V.; Di Tizio, V.; Radisic, M. Angiopoietin-1 peptide QHREDGS promotes osteoblast differentiation, bone matrix deposition and mineralization on biomedical materials. *Biomater. Sci.* **2014**, *2* (10), 1384–1398.

(43) Rosenberg, M.; Shilo, D.; Galperin, L.; Capucha, T.; Tarabieh, K.; Rachmiel, A.; Segal, E. Bone Morphogenic Protein 2-Loaded Porous Silicon Carriers for Osteoinductive Implants. *Pharmaceutics* **2019**, *11* (11), 602.

(44) Ming, P.; Rao, P.; Wu, T.; Yang, J.; Lu, S.; Yang, B.; Xiao, J.; Tao, G. Biomimetic Design and Fabrication of Sericin-Hydroxyapatite Based Membranes With Osteogenic Activity for Periodontal Tissue Regeneration. *Front. Bioeng. Biotechnol.* **2022**, *10*, No. 899293.

(45) Wang, T.; Yang, X.; Qi, X.; Jiang, C. Osteoinduction and proliferation of bone-marrow stromal cells in three-dimensional poly (epsilon-caprolactone)/ hydroxyapatite/collagen scaffolds. *J. Transl. Med.* **2015**, *13*, 152.

(46) Yamamoto, K.; Kishida, T.; Sato, Y.; Nishioka, K.; Ejima, A.; Fujiwara, H.; Kubo, T.; Yamamoto, T.; Kanamura, N.; Mazda, O. Direct conversion of human fibroblasts into functional osteoblasts by defined factors. *Proc. Natl. Acad. Sci. U.S.A.* **2015**, *112* (19), 6152–6157.

(47) Sun, C.; Du, K.; Fang, C.; Bhattarai, N.; Veisoh, O.; Kievit, F.; Stephen, Z.; Lee, D.; Ellenbogen, R. G.; Ratner, B.; Zhang, M. PEG-mediated synthesis of highly dispersive multifunctional superparamagnetic nanoparticles: their physicochemical properties and function in vivo. *ACS Nano* **2010**, *4* (4), 2402–2410.

(48) Seo, W.; Lee, S.; Tran, P. T.; Ngo, T. Q.; Kim, O.; Le, T. H.; Dang, N. H.; Hwangbo, C.; Min, B. S.; Lee, J. H. 3-Hydroxyolean-12-en-27-oic Acids Inhibit RANKL-Induced Osteoclastogenesis in Vitro and Inflammation-Induced Bone Loss in Vivo. *Int. J. Mol. Sci.* **2020**, *21* (15), 5240.

(49) Heo, J.; Kim, M.; Kim, J. H.; Shin, H.; Lim, S. E.; Jung, H. S.; Sohn, Y.; Ku, J. Effect of Taraxaci Herba on Bone Loss in an OVX-Induced Model through the Regulation of Osteoclast Differentiation. *Nutrients* **2022**, *14* (20), 4354.

(50) Zhao, F.; Gao, X.; Ge, X.; Cui, J.; Liu, X. Cyanidin-3-o-glucoside (C3G) inhibits vascular leakage regulated by microglial activation in early diabetic retinopathy and neovascularization in advanced diabetic retinopathy. *Bioengineered* **2021**, *12* (2), 9266–9278.